Structuring Interdigitated Back Contact Solar Cells Using the Enhanced Oxidation Characteristics Under Laser-Doped Back Surface Field Regions

Kuruganti, Vaibhav V.; Isabella, Olindo; Mihailetchi, Valentin D.

DOI
10.1002/pssa.202300820

Publication date
2024

Document Version
Final published version

Published in
Physica Status Solidi (A) Applications and Materials Science

physica status solidi a
www.pss-a.com

Structuring Interdigitated Back Contact Solar Cells Using the Enhanced Oxidation Characteristics Under Laser-Doped Back Surface Field Regions

Vaibhav V. Kuruganti, Olindo Isabella, and Valentin D. Mihailetchi*

Interdigitated back contact (IBC) architecture can yield among the highest silicon wafer-based solar cell conversion efficiencies. Since both polarities are realized on the rear side, there is a definite need for a patterning step. Some of the common patterning techniques involve photolithography, inkjet patterning, and laser ablation. This work introduces a novel patterning technique for structuring the rear side of IBC solar cells using the enhanced oxidation characteristics under the locally laser-doped n^{++} back surface field (BSF) regions with high-phosphorous surface concentrations. Phosphosilicate glass layers deposited via $POCl_3$ diffusion serve as a precursor layer for the formation of local heavily laser-doped n^{++} BSF regions. The laser-doped n^{++} BSF regions exhibit a 2.6-fold increase in oxide thickness compared to the nonlaser-doped n^{+} BSF regions after undergoing high-temperature wet thermal oxidation. The utilization of oxide thickness selectivity under laser-doped and nonlaser-doped regions serves two purposes in the context of the IBC solar cell, first patterning rear side and second acting as a masking layer for the subsequent boron diffusion. Proof-of-concept solar cells are fabricated using this novel patterning technique with a mean conversion efficiency of 20.41%.

1. Introduction

In the early 1970s, Schwartz and Lammert developed the first interdigitated back contact (IBC) solar cells.[1] In the nascent stages, IBC cell design was optimized for concentrator application to cope with the high intensities of incoming energy fluxes and the related high current densities.[2] Due to its inherent advantages, this cell architecture was later adapted for one sun application.[3] In the IBC cell architecture, contacts for both types of polarities are placed on the nonilluminated side of the solar cell. The most obvious advantage of IBC cells over conventional both-side contact solar cells is the elimination of any optical shading losses caused by the metal finger and busbars on the front side, allowing the solar cells to boast a higher short-circuit current density J_{sc}. A more comprehensive range of front surface texturing and light trapping schemes could be adopted on the front surface of the IBC structure, as there is no need for heavily doped regions like in the case of both side contact solar cells.[4] Another considerable advantage is the reduced complexity of cell interconnection inside the module.[5] The design architecture is perfect for mechanically stacked tandem cells with higher-bandgap technologies, like perovskites, in a three-terminal configuration.[6] Research groups and companies use IBC architecture worldwide to make high-efficiency solar cells because of the abovementioned benefits. In research and development, Kaneka Corporation reported a conversion efficiency of 26.7% for its heterojunction IBC,[7] and ISFH reported a conversion efficiency of 26.1% on its POLO IBC solar cells.[8] At the industrial scale, SunPower reported an efficiency of 25% on the SunPower X-Series technology,[9] and SPIC reported an efficiency above 23.5% on its low-cost bifacial IBC ZEBRA technology.[10]

Since both polarities are located on the rear side of the IBC solar cell concept, there is a definite need for a patterning step. Some of the first IBC solar cells developed in the early 1980s and 1990s used photolithography techniques for patterning on the rear side.[11] Photolithography is a well-established technique that uses light to produce minutely patterned thin films of suitable material over a substrate to protect selected regions (mask) during the subsequent etching, deposition, or implantation process. Franklin et al.[12] reported an efficiency of 24.4% on their IBC solar cells, which were patterned using photolithography. The fabrication of this cell had as many as four photolithography steps. Besides photolithography, alternative patterning techniques include inkjet patterning of a resist layer followed by wet chemical etching and aerosol jet printing.[13,14] All the methods

V. V. Kuruganti, V. D. Mihailetchi
R&D Solar Cells
International Solar Energy Research Center (ISC) Konstanz
Rudolf-Diesel-Str. 15, Konstanz D-78467, Germany
E-mail: vaibhav.kuruganti@isc-konstanz.de

O. Isabella
Photovoltaic Materials and Devices (PVMD) Group
Delft University of Technology
Mekelweg 4, Delft 2628 CD, Netherlands

The ORCID identification number(s) for the author(s) of this article can be found under https://doi.org/10.1002/pssa.202300820.

DOI: 10.1002/pssa.202300820

mentioned above require multiple wet bench processing steps and sophisticated equipment, making them not viable for application in the photovoltaic (PV) industry. In recent years, Dullweber et al.[15] showed an elegant way of locally depositing one polarity of the polysilicon (poly-Si) layer using plasma-enhanced chemical vapor deposition (PECVD) through a glass-based shadow mask.

Laser ablation has been one of the most successful approaches for patterning the rear side in IBC solar cells.[10,16] The use of the laser ablation technique for the fabrication of IBC solar cells has been reported by Engelhart et al.[16] and O'Sullivan et al.[17] using a picosecond laser for the ablation of dielectric layers like SiO_2. In addition, Kronz et al.[18] demonstrated SiN_x ablation using a nanosecond laser. However, laser ablation can cause unintentional laser-induced damage such as surface melting, heat-affected zones, microcracks, and point defects on the underlying silicon layer, negatively affecting solar cell performance.[19] Hence an additional wet bench step is introduced for laser-induced damage removal before the subsequent high-temperature step.

Dahlinger et al.[20] presented an innovative technique using laser doping to enable local doping of IBC cells without masking layers.[21] The laser doping was used to form the local n^{++} back surface field (BSF) and a local p^{++} emitter with high spatial resolution without the necessity of any masking. Alternatively, Franklin et al.[12] and Zieliński et al.[22] used laser doping to form one polarity and laser ablation for the patterning and aligned contact formation using the nanosecond (ns) laser.

In this work, we use the enhanced oxidation rates under locally laser-doped n^{++} BSF regions for patterning the rear side of IBC solar cells. We perform laser doping on $POCl_3$ diffused samples using PSG glass as a precursor layer. Due to the higher oxidation rates under the heavily doped n^{++} BSF regions,[23,24] upon wet thermal oxidation at 850 °C for 30 min, we were able to grow a thick SiO_2 layer of 125 nm under laser-doped regions, as compared to a thin SiO_2 layer of 48 nm on the nonlaser doped regions. The selectivity in the thickness of the SiO_2 layer under lasered and nonlasered regions was used for patterning the rear side of the IBC solar cells. It was also observed that the remaining SiO_2 layer under the laser-doped regions after patterning was sufficient to act as a dopant barrier for the subsequent boron diffusion process, making the processing of the IBC solar cells robust and streamlined.

2. Results and Discussion

2.1. Deal–Grove Model Simulation Study

Silicon oxide has a profound place in the fabrication of PVs and the integrated circuit industry. SiO_2 is primarily a passivation layer to passivate the surface dangling bonds on c-Si. It is also used as an insulator between semiconductor devices and a masking layer to act as a dopant barrier.[25] Due to its high etch selectivity in alkaline solution compared to c-Si,[26] it is also used in the semiconductor industry for patterning purposes.

SiO_2 is grown in a furnace by supplying oxygen (O_2) to the c-Si surface and reacting at high temperatures. Bruce Deal and Andy Grove (of Fairchild Semiconductor) developed the first straightforward kinetic model for SiO_2 growth in the early 1960s.[24] Ho et al.[27] studied the enhanced oxidation effects in the heavily doped n^{++} c-Si substrate. The observed phenomenon is attributed to the shifting of Fermi level toward the conduction band in heavily doped n^{++} c-Si substrate, causing an increase in the equilibrium concentration of point defects or vacancies in the silicon. These point defects act as reaction sites for the chemical reaction converting Si to SiO_2, enhancing the linear rate constant, which is interface reaction dependent.[28] Hence the oxidation rates are much higher for a heavily doped n^{++} c-Si substrate than for a lightly doped c-Si substrate.

In this study, simulations were performed to understand the influence of phosphorous surface concentration N_s on the growth dynamics of the SiO_2 layer using Integrated Circuits and Electronics group Computerized Remedial Education and Mastering (ICECREM) software which uses the Deal–Grove model.[29] Simulations of wet and dry oxidation were done by varying the substrate doping from 1×10^{15} to 7×10^{19} cm^{-3} for 30 min at 850 °C, as represented in **Figure 1**.

During dry oxidation, the silicon wafer reacts in a pure oxygen gas atmosphere (O_2) at elevated temperatures. Based on the data presented in Figure 1, it is evident that increasing the N_s results in a sufficient selectivity in SiO_2 thickness during dry oxidation. However, it is important to note that the oxide growth rate is significantly low, rendering it unsuitable for selective etch back in an acidic solution. Additionally, the retained oxide after patterning is insufficient to serve as a masking layer during subsequent BBr_3 diffusion. During wet oxidation, the silicon wafer reacts in a water vapor atmosphere (H_2O) at elevated temperatures. Compared to dry thermal oxidation, much thicker oxides can be formed using wet thermal oxidation. The observed phenomenon is due to the higher solubility of H_2O in Si than in the O_2 molecule.[24] Hence the thicker oxides obtained using wet thermal oxidation can be used for our patterning application.

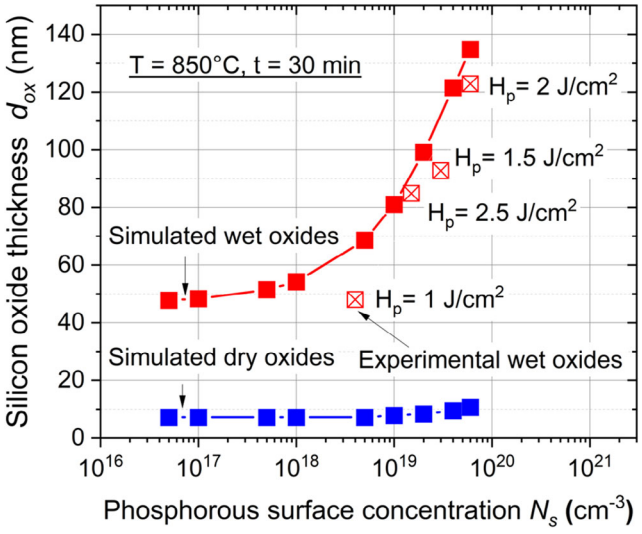

Figure 1. Influence of phosphorous surface dopant concentration (N_s) on the oxide thickness (d_{ox}) for wet and dry thermal oxidation simulated using the Deal–Grove model represented by solid squares and the actual measured d_{ox} after wet thermal oxidation at different laser pulse energy densities H_p as a function of different N_s represented with open squares.

In theory, we observe high selectivity (1:2.8) of SiO_2 thickness between lightly $1 \times 10^{15}\,cm^{-3}$ and heavily doped $7 \times 10^{19}\,cm^{-3}$ silicon substrates. Increasing the substrate phosphorus level strongly affects the interface reaction rate.[27]

2.2. Influence of Laser Doping Settings on the Sheet Resistance and Oxidation Rates of n^{++} c-Si

Figure 2a illustrates the impact of laser pulse energy density H_p on the R_{sh} of laser-doped n^{++} c-Si (left) and the SiO_2 thickness d_{ox} under laser-doped regions after wet thermal oxidation (right). The resulting curves can be interpreted into three separate zones, as observed by Hassan et al.[30] for laser doping of crystalline silicon from boron precursor layers. In zone-I ($0\,J\,cm^{-2} < H_p < 2\,J\,cm^{-2}$), the laser energy is less than the melting thresholds of Si; thus, doping is not possible. Therefore, we detect no change in the R_{sh} and d_{ox} values in this zone-I. In zone-II ($1\,J\,cm^{-2} < H_p < 2\,J\,cm^{-2}$), a linear decrease in R_{sh} with increasing H_p is seen, which indicates that the number of phosphorous atoms in the doped layer also increases linearly. Interestingly, also in zone-II, we observe a linear increase in the d_{ox} from 48 nm at $1\,J\,cm^{-2}$ to almost 123 nm at $2\,J\,cm^{-2}$. This increase in the d_{ox} after wet thermal oxidation is attributed to increased N_s. From Figure 2b, it can be observed that the N_s increases from $4 \times 10^{18}\,cm^{-3}$ at $1\,J\,cm^{-2}$ to $6 \times 10^{19}\,cm^{-3}$ (more than one order of magnitude) at $2\,J\,cm^{-2}$. Hence we can conclude that the decrease in R_{sh} of zone-II can be mainly attributed to the alteration of the dopant concentration at the surface and marginally due to a deeper junction.

Progressing to zone III ($H_p > 2\,J\,cm^{-2}$), the R_{sh} decreases marginally and then saturates at $75\,\Omega\,sq^{-1}$ with increasing laser H_p. In this zone, we observe that the decrease in R_{sh} is dominantly due to the deeper junction whereas the N_s gradually starts to decrease with increasing laser H_p. d_{ox} after wet thermal oxidation starts to decrease in the zone III and this can be explained by the decreased N_s. Indeed, as seen in Figure 2b, we observe the decrease in the N_s from $6 \times 10^{19}\,cm^{-3}$ at $2\,J\,cm^{-2}$ to $1.5 \times 10^{19}\,cm^{-3}$ at $2.5\,J\,cm^{-2}$. In this zone, we start evaporating the precursor layers and partially evaporating parts of the doped silicon surface, lowering the N_s at the silicon interface. A similar observation was seen in Hassan et al.[30]

The experimental measured d_{ox} after laser doping and wet thermal oxidation were compared to the simulated wet thermal oxidation d_{ox} and are depicted in Figure 1 with an open red box. We observe that all the experimental measured d_{ox} is lower than that of the simulated d_{ox}. One explanation for the observed discrepancy is the phosphorous active concentration doping profile being different for experimental and simulated results. All the simulated d_{ox} are calculated, assuming a uniform rectangular doping profile, while the experimental laser doping has a complementary error function doping profile. During oxidation, silicon is partially consumed to form SiO_2. According to the literature, 54% of SiO_2 grows on the c-Si substrate, and the remaining 46% grows below the original c-Si substrate, thereby partially consuming Si during oxidation.[24] Hence for a very shallow laser-doped profile with a steep decrease in the dopant concentration (like $1\,J\,cm^{-2}$), we observe a much higher deviation between simulated and measured d_{ox}. In comparison, to the deeper laser-doped profile with a uniform doping profile (like $2.5\,J\,cm^{-2}$), we observe good agreement with the simulated values.

2.3. The Process Sequence of IBC Solar Cells Using the Novel Patterning Technique

The previous section established that we could increase the phosphorous concentration N_s at localized regions by fine tuning the laser doping parameters. The enhanced oxidation rates under these selectively laser-doped n^{++} BSF regions can be used for patterning IBC solar cells. To investigate the feasibility of this patterning approach, a process sequence was formulated and is depicted in **Figure 3**b.

The phosphorous-doped Cz-Si wafers used for solar cell fabrication were $180 \pm 10\,\mu m$ thick with a base resistivity (ρ_b) $= 4 \pm 0.5\,\Omega\,cm$ and M2 size. The process sequence starts with saw damage removal and Piranha chemical cleaning. Conventional tube diffusion at atmospheric pressure using $POCl_3$ liquid precursor was used to deposit a phosphosilicate

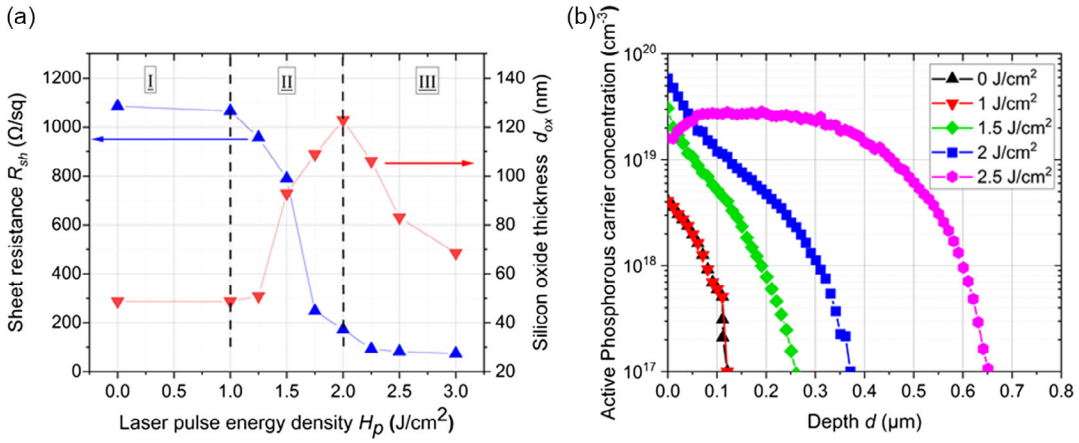

Figure 2. Electrical characteristics of the n^{++} laser-doped regions. a) Influence of laser pulse energy density H_p on the sheet resistance R_{sh} and thickness d_{ox} of SiO_2 layer after wet thermal oxidation and b) active dopant concentration profiles of the n^{++} regions, determined from ECV measurements, for different H_p.

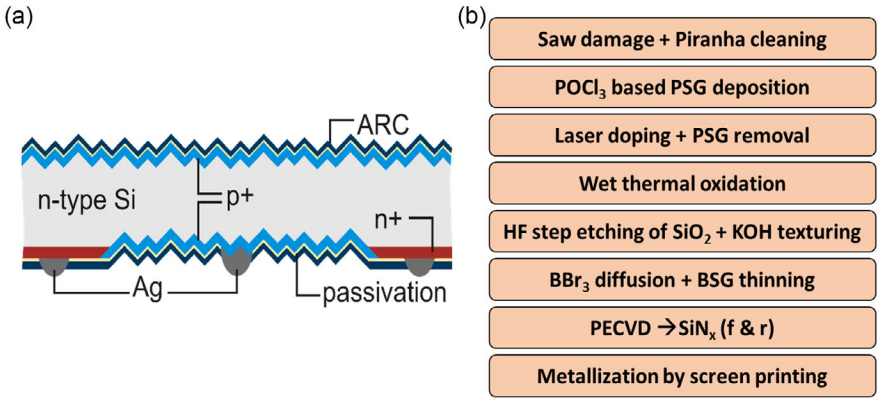

Figure 3. a) A schematic cross-section view of the resulting IBC cell and b) fabrication steps of IBC solar cells using the novel patterning technique.

glass (PSG) layer on the c-Si substrate, which will be later used as a precursor for laser doping. The best laser doping settings obtained from the previous section were used to selectively laser dope 33% of the area on the back side of the wafer, forming the 75 Ω sq^{-1} n^{++} back surface field (BSF) region. The precursor PSG layer is removed in the acidic HF bath before wet thermal oxidation at 850 °C for 30 min. After the high-temperature step, we grow a thick SiO_2 under the BSF regions and a thin SiO_2 under nonlaser-doped regions. The SiO_2 is controllably etched back in the HF solution in the subsequent etching step. The process is interrupted when the thin SiO_2 layer under nonlaser-doped regions is completely removed. The samples then undergo a texturing step during which the nonlasered regions on the rear side and the complete front side get textured, whereas, under the laser-doped BSF regions, the thick SiO_2 acts as an etch stop. A standard tube diffusion system at atmospheric pressure using BBr_3 liquid precursor was used to form the 150 Ω sq^{-1} p$^+$ emitter on the rear and 150 Ω sq^{-1} p$^+$ front floating emitter (FFE) on the front. The thick SiO_2 under the laser-doped regions prevents the boron from reaching the BSF interface and acts as a self-making layer. The BBr_3 drive-in phase is done in a partial oxygen environment, thereby growing a homogeneous in situ thermal SiO_2 at the Si interface. In the paper by Mihailetchi et al.,[31] we demonstrate that this in situ-grown thermal SiO_2 can be used as a buffer layer to etch back the BSG layer entirely in an HF wet bench step due to the selectivity in the etching rates of the dopant glass layer and in situ-grown thermal glass layer. The remaining in situ thermal SiO_2 was capped with a PECVD SiN_x to passivate both p$^+$ and n^{++} polarities.[32] The metallization of these solar cells was achieved using our best-known method of screen printing and firing through a process from ZEBRA technology.[5] The schematic representation of the IBC solar cells fabricated using the novel patterning sequence is depicted in Figure 3a.

2.4. Optimization of the Process Sequence and Solar Cell Results

Successful implementation of this process sequence to fabricate solar cells critically depends on the two key steps after wet thermal oxidation, during which the SiO_2 under nonlasered regions has to be completely removed. At the same time, under the laser-doped regions, one has to retain sufficient SiO_2 thickness to withstand the texturing step and the subsequent BBr_3 diffusion. Hence these two processing steps are studied in detail.

2.4.1. HF Etching of SiO_2 and KOH Texturing

The goal during the step etching in acidic HF solution is to completely etch the 48 nm-thick SiO_2 under the nonlaser-doped regions and still retain a thick-enough SiO_2 under laserdoped regions to act as a masking layer for the subsequent texturing and BBr_3 diffusion processes. Since we have a difference in the oxidation rates under lasered and nonlasered regions for the same wet thermal oxidation duration, the etching rates of the SiO_2 under both regions were tested. To investigate the etch rate of the different SiO_2 layers, the wafers were immersed in 2-vol% HF acid solution for a defined period, followed by thickness measurement. The thickness t versus etching time slope was used to determine the etching rate. The etching rate of laser-doped regions was determined to be 0.17 nm s^{-1}, whereas that of nonlaser-doped regions was 0.16 nm s^{-1}, which is quite comparable. SiO_2-obtained etching rates were comparable with Spierings et al.[25] at an etchant concentration of 2-vol%. Using the knowledge of the etching rates, the samples underwent a wet bench processing in an HF bath for 420 s, during which the SiO_2 under the nonlasered part was completely etched and retained 75 nm-thick SiO_2 under the laser-doped n^{++} BSF regions.

The subsequent texturing step happens in the batch-type RENA wet bench. The etching rate of thermally grown SiO_2 = is 200–400 times slower than that of c-Si in an alkaline texturing bath at 80 °C.[25] Hence, the nonlasered regions on the rear and the complete front side are textured, leaving the laser-doped n^{++} BSF region protected from texturing using the SiO_2 etch stop layer. The samples are quickly cleaned in the HF solution during the standard batch-type RENA wet bench texturing. The texturing step removed ≈3.5 µm of c-Si under nonlaser-doped regions. In contrast, only 20 nm of SiO_2 under the laser-doped n^{++} BSF regions were etched. Hence during the texturing process using the self-masked SiO_2 under laser-doped BSF regions, we pattern the rear side and texture the front side of the IBC solar cells.

2.4.2. BBr_3 Diffusion and BSG Thinning

BBr_3 diffusion step was used to form the p^+ emitter on the rear as well as on the front side (FFE) of the solar cells. During BBr_3 diffusing, we wanted to investigate if the 55 nm-thick SiO_2 retained under the laser-doped n^{++} BSF regions after texturing was sufficient to act as a masking layer. To study the thickness of SiO_2 needed to function as a masking layer for our BBr_3 tube diffusion recipe, we used the SiO_2 thickness control samples specified in the experimental section.

Figure 4a shows the results of the R_{sh} as a function of d_{ox}, and Figure 4b shows the boron-active doping concentration profile measured using ECV on samples with different d_{ox} masking layer thicknesses that underwent BBr_3 diffusion. An eddy current sensor was used to measure the layer stack's sheet resistance (i.e., the parallel summation of the emitter and base R_{sh}). The as-cut bare wafer used in this study was a p-type wafer with a base resistivity $= 5 \pm 0.5\ \Omega$.cm, corresponding to a doping concentration $= 2.5 \times 10^{15}\ cm^{-3}$ and the $R_{sh} = 350 \pm 10\ \Omega\ sq^{-1}$.

For samples without SiO_2, there is no blocking layer; hence, a heavily doped p^+ region with comparatively high boron $N_s = 2 \times 10^{19}\ cm^{-3}$ and deep junction depth $D_p = 0.6\ \mu m$ was formed. Due to the heavy doping of the emitter layers, the R_{sh} of the layer stack decreases to $60\ \Omega\ sq^{-1}$, as shown in Figure 4a.

For $1\ nm < d_{ox} < 10\ nm$, the total R_{sh} of the layers increases linearly from 60 to $250\ \Omega\ sq^{-1}$ with the increase in d_{ox}. In this regime, the dopant penetrates through the SiO_2, forming a heavily doped emitter region. The increase in the R_{sh} values with increasing d_{ox} indicates that with thicker oxide, we tend to block boron from reaching the c-Si interface though not completely. For this thickness range, as shown in Figure 4b, the N_s decreased from $2 \times 10^{19}\ cm^{-3}$ at 0 nm = SiO_2 to $9 \times 10^{18}\ cm^{-3}$ at 10 nm of SiO_2, with no significant change in the junction depths.

For d_{ox} in the range between 10 and 20 nm, the total R_{sh} increases from 250 to $350\ \Omega\ sq^{-1}$. After a further increase in the thickness of SiO_2, the total R_{sh} saturates at $350\ \Omega\ sq^{-1}$, which is then limited by the R_{sh} of the undiffused wafer. Another important observation from Figure 4b is for the measurements with a SiO_2 thickness = 15 nm; though the dopant penetrates through the SiO_2 layer, it decreases the overall dopant N_s by three orders of magnitudes to almost $2 \times 10^{16}\ cm^{-3}$ with a very shallow doping profile. However, there is no detectable boron doping profile for the samples with SiO_2 thickness of more than 20 nm, indicating the thickness of SiO_2 is sufficient to completely block the BBr_3 diffusion, as also confirmed from the R_{sh} measurements shown in Figure 4b. Hence, we can conclude that the 55 nm-thick SiO_2 under the laser-doped n^{++} BSF region is sufficiently thick to block the boron atoms from reaching the BSF interface.

2.4.3. Solar Cell Results

The proof-of-concept solar cells were fabricated using the process sequence depicted in Figure 3a. The (current-voltage) *I–V* parameters were measured using a HALM flash tester and are listed in **Table 1**. A median cell efficiency of 20.09%, with a maximum efficiency of 20.41%, was obtained. The results obtained from the injection-dependent lifetime measurements conducted using quasisteady-state photoconductance on symmetrical lifetime samples revealed a lower bulk lifetime (τ_{bulk}) under the phosphorous laser-doped BSF, as compared to the boron emitter regions with comparable emitter saturation current density (J_{0e}) values. The observed decrease in bulk time in the phosphorous laser-doped BSF sections is speculated to be due to two potential factors: laser-induced bulk damage during the laser doping step and the formation of oxidation-induced stacking faults in the subsequent wet thermal oxidation step.[19,33] Although the achieved cell efficiency is not particularly high, as the fabrication process was not optimized, it demonstrates the functionality of the novel patterning method to fabricate IBC solar cells.

Table 1. Summary of (current–voltage) *I–V* characteristics namely: open-circuit voltage (V_{oc}), short-circuit current (J_{sc}), fill factor (FF), and conversion efficiency (η) of the IBC solar cells.

Group	V_{oc} [mV]	J_{sc} [mA cm^{-2}]	FF [%]	η [%]
Median	652.3	40.22	76.79	20.08
Maximum	656.6	40.38	77.39	20.42

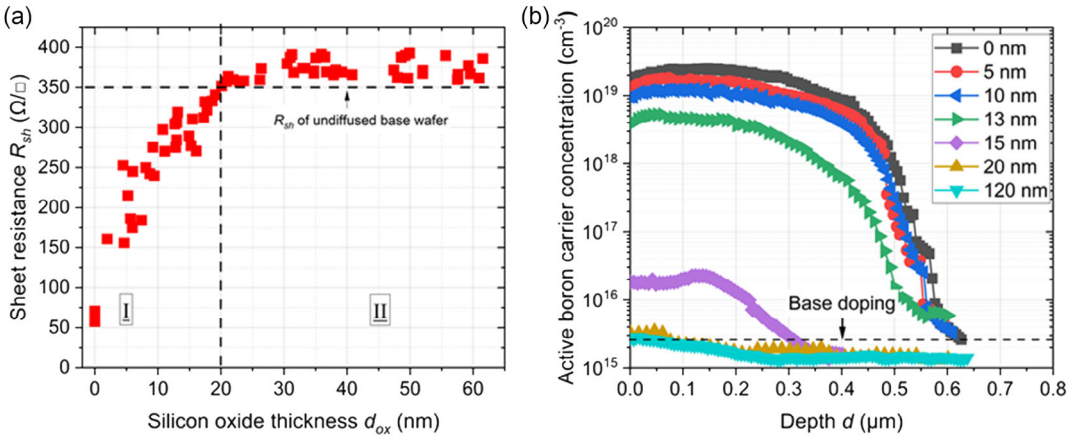

Figure 4. a) Influence of the masking SiO_2 thickness d_{ox} on the sheet resistance R_{sh} of the wafers after BBr_3 diffusion. b) Influence of the masking SiO_2 thickness d_{ox} on the active boron carrier concentration profiles.

The utilization of the increased oxidation characteristics of n^{++} Si layers in the novel patterning technique is not limited solely to diffused junctions, as demonstrated in this study. It may also be applied to the state-of-the-art passivating contact IBC solar cells.

There are several fundamental distinctions that must be considered when implementing this method on poly-Si layers. 1) Grain boundaries have a crucial role in facilitating the diffusion of phosphorous atoms, hence enabling a high dopant diffusivity in case of poly-Si compared to crystalline silicon.[34] Hence, the phosphorous diffusion should be optimized such that low phosphorous ($<5 \times 10^{18}\,cm^{-3}$) should be incorporated in the poly-Si layer during $POCl_3$ diffusion and then using the laser doping we can selectively increase the phosphorous concentration ($>7 \times 10^{19}\,cm^{-3}$) such that we can get enough selectively in the oxide thickness post wet thermal oxidation. 2) The anticipated threshold fluence required for laser doping is expected to be lower for poly-Si layers in comparison to the c-Si substrate, owing to the higher absorption coefficient exhibited by the former.[35] Furthermore, it is essential to carefully adjust the laser doping settings in order to avoid any potential damage to the interfacial oxide layer and hence maintain the desired passivation quality.[36] 3) During oxidation, due to the stress induced by the grain boundaries, the oxidation rates of the poly-Si are initially faster than the crystalline silicon.[37] Also during oxidation, silicon is partially consumed to form SiO_2. As a result, it is necessary to start with thicker poly-Si layers in order to end with poly-Si layer thicknesses that can be contacted without the metal paste spiking through.[38]

3. Conclusion

This article presents a novel patterning technique for fabricating IBC solar cells. We have demonstrated that using the enhanced oxidation rates under the local laser-doped n^{++} BSF regions, we can pattern the rear side of the IBC solar cells and mask the laser-doped n^{++} BSF regions from the subsequent BBr_3 diffusion.

We have investigated the influence of the laser pulse energy density on the sheet resistance of the laser-doped n^{++} c-Si and the SiO_2 thickness d_{ox} under laser-doped regions after wet thermal oxidation. It was concluded that upon fine tuning H_p, we could locally enhance the phosphorous N_s by more than one order of magnitude. Wet thermal oxidation would yield thicker and thinner SiO_2 under laser and nonlasered regions, respectively, with a 2.6 time selectivity under laser-doped regions. This property can be used to an advantage if the SiO_2 is then controllably etched back into the HF solution. After removing the thin SiO_2 layer beneath the nonlaser-doped regions, the etching process is interrupted. The remaining SiO_2 layer under the laser-doped regions can be used as an etch stop layer under the BSF regions from the texturing step, during which the rear side is patterned and subsequently acts as a dopant barrier for the BBr_3 diffusion step, during which the emitter is formed on the front and rear side. The proof-of-concept solar cells were fabricated with novel patterning techniques and have demonstrated a conversion efficiency of 20.41%.

4. Experimental Section

All the process equipment used was industrial or industrial like, such as Centrotherm tube diffusion furnaces for BBr_3 diffusion, $POCl_3$ diffusion, and thermal oxidation. Hydrofluoric acid etching was performed in a 2% HF solution, and alkaline etching was carried out on a batch-type RENA wet bench. Local laser treatment was performed in industrially feasible high-throughput tools. The SiN_x layers were deposited using the Centrotherm PECVD system and fired in a Centrotherm fast-firing furnace.

Sheet Resistance (R_{sh}) Samples: The R_{sh} samples were used to investigate the influence of different laser parameters on the electrical properties and the subsequent oxide growth rates under the laser-doped areas. We used the M2 wafer format, *p*-type Czochralski wafer with a thickness = 180 ± 10 µm, and a base resistivity (ρ) = 1 ± 0.5 Ω cm. The samples underwent saw damage etching and Piranha cleaning before the high-temperature $POCl_3$ tube diffusion. For this study, the $POCl_3$ recipe was optimized only to have a deposition phase without any high-temperature drive-in step. Due to the lack of the drive-in phase in $POCl_3$ diffusion, most of the phosphorous was present in the PSG layer. All samples were then laser treated by a frequency-doubled Nd: YVO_4 nanosecond ns pulse laser with a wavelength = 532 nm. A pulse duration (τ_p) = 60–160 ns was used to create the laser-doped regions with various laser settings. The laser had a flat top profile with a rectangular spot size = 300 × 600 µm^2. The samples were cleaned in a 2-vol% HF solution to remove the precursor glass layer before the subsequent high-temperature wet thermal oxidation process for 30 min at 850 °C. The thickness of the SiO_2 layer under the different laser doping settings was carried out with an SE800-PV ellipsometer. The SiO_2 was etched in a 2-vol% HF acid solution at room temperature to evaluate the electrical characteristics of the laser-doped regions, namely, R_{sh} and doping profile. GP Solar's 4Tests PRO was used to measure the R_{sh} using a four-point probe method, and a wafer profiler electrochemical capacitance–voltage (ECV) tool was used to measure the active dopant profile.

Silicon Oxide (SiO_2) Thickness Control Samples: The SiO_2 thickness control samples consisted of flat c-Si wafers with different SiO_2 thicknesses ranging from 5 to 65 nm. These samples were used to investigate the required thickness of SiO_2 for functioning as a diffusion barrier against boron diffusion in the BBr_3 tube diffusion step. For these samples, we used p-type Cz-Si wafers with base resistivity = 5 ± 0.5 Ω cm and a nominal thickness = 180 µm. The samples underwent saw damage etching and Piranha cleaning before the high-temperature wet thermal oxidation step. The wet thermal oxidation was done for 45 min at 950 °C to grow 185 ± 2 nm SiO_2 on the wafers. To investigate the etch rate of the thermal grown SiO_2, the wafers were immersed in 2-vol% HF acid solution for a defined period, followed by thickness measurement. The etching rate was determined from the slope of the thickness versus the etching time. Using the knowledge of the etching rate, each wafer was then separately thinned down to specific thicknesses ranging from 5 nm to 65 nm accordingly. These samples with different SiO_2 thicknesses were processed in the BBr_3 tube diffusion. Like sheet resistance control samples, the glass layers on the c-Si substrate were completely removed in a 2-vol% HF solution to monitor the electrical properties.

Acknowledgements

This work was funded by the German Federal Ministry for Economic Affairs and Energy within the research project "RALPH" (contract no. 03EE1018C).

Conflict of Interest

The authors declare no conflict of interest.

Data Availability Statement

The data that support the findings of this study are available from the corresponding author upon reasonable request.

Keywords

interdigitated back contact solar cells, laser doping, patterning techniques, SiO_2 as diffusion barriers

Received: October 26, 2023
Revised: December 21, 2023
Published online:

[1] R. Schwartz, M. Lammert, in *1975 International Electron Devices Meeting*, IEEE, Piscataway, NJ **1975**, pp. 350–352.
[2] M. Ahmad, *Sol. Cells* **1988**, *25*, 53.
[3] R. A. Sinton, R. M. Swanson, *IEEE Trans. Electron Devices* **1990**, *37*, 348.
[4] T. Rahman, R. S. Bonilla, A. Nawabjan, P. R. Wilshaw, S. A. Boden, *Sol. Energy Mater. Sol. Cells* **2017**, *160*, 444.
[5] G. Galbiati, H. Chu, V. D. Mihailetchi, J. Libal, R. Kopecek, in *Proc. 7th WCPEC*, IEEE, United States **2018**, pp. 1540–1543.
[6] P. Tockhorn, P. Wagner, L. Kegelmann, J.-C. Stang, M. Mews, S. Albrecht, L. Korte, *ACS Appl. Energy Mater.* **2020**, *3*, 1381.
[7] K. Yoshikawa, W. Yoshida, T. Irie, H. Kawasaki, K. Konishi, H. Ishibashi, T. Asatani, D. Adachi, M. Kanematsu, H. Uzu, K. Yamamoto, *Sol. Energy Mater. Sol. Cells* **2017**, *173*, 37.
[8] C. Hollemann, F. Haase, M. Rienäcker, V. Barnscheidt, J. Krügener, N. Folchert, R. Brendel, S. Richter, S. Großer, E. Sauter, J. Hübner, M. Oestriech, R. Peibst, *Sci. Rep.* **2020**, *10*, 658.
[9] D. D. Smith, P. Cousins, S. Westerberg, R. D. Jesus-Tabajonda, G. Aniero, Y. Shen, *IEEE J. Photovolt.* **2014**, *4*, 1465.
[10] R. Kopecek, J. Libal, J. Lossen, V. D. Mihailetchi, H. Chu, C. Peter, F. Buchholz, E. Wefringhaus, A. Halm, J. Ma, L. Jianda, G. Yonggang, Q. Xiaoyong, W. Xiang, D. Peng, in *47th IEEE Photovoltaic Specialists Conference*, IEEE, Piscataway, NJ **2020**, pp. 1008–1012.
[11] F. W. Sexton, C. M. Garner, J. L. Rodriguez, *J. Electrochem. Soc.* **1982**, *129*, 2624.
[12] E. Franklin, K. Fong, K. McIntosh, A. Fell, A. Blakers, T. Kho, D. Walter, D. Wang, N. Zin, M. Stocks, et al., *Prog. Photovolt.: Res. Appl.* **2016**, *24*, 411.
[13] As. J. Lennon, A. W. Ho-Baillie, S. R. Wenham, *Sol. Energy Mater. Sol. Cells* **2009**, *93*, 1865.
[14] R. Woehl, M. Horteis, S. W. Glunz, *Adv. Optoelectron.* **2008**, *1–7*, 2008.
[15] T. Dullweber, M. Stöhr, C. Kruse, F. Haase, M. Rudolph, B. Beier, P. Jäger, V. Mertens, R. Peibst, R. Brendel, *Sol. Energy Mater. Sol. Cells* **2020**, *212*, 110586.
[16] P. Engelhart, N.-P. Harder, R. Grischke, A. Merkle, R. Meyer, R. Brendel, *Prog. Photovolt.: Res. Appl.* **2007**, *15*, 237.
[17] B. O'Sullivan, M. Debucquoy, S. Singh, A. U. De Castro, M. R. Payo, N. Posthuma, I. Gordon, J. Szlufcik, J. Poortmans, *28th EU-PVSEC*, WIP, Munich **2013**, pp. 956–960.
[18] A. Knorz, M. Peters, A. Grohe, C. Harmel, R. Preu, *Prog. Photovolt.: Res. Appl.* **2009**, *17*, 127.
[19] J. M. Y. Ali, V. Shanmugam, A. Khanna, P. Wang, N. Balaji, R. V. Tabajonda, D. J. Perez, A. G. Aberle, T. Mueller, *Sol. Energy Mater. Sol. Cells* **2019**, *192*, 117.
[20] M. Dahlinger, B. Bazer-Bachi, T. C. Röder, J. R. Köhler, R. Zapf-Gottwick, J. H. Werner, *Energy Procedia* **2013**, *38*, 250.
[21] U. Jäger, A. Wolf, B. Steinhauser, J. Benick, J. Nekarda, R. Preu, in *Laser Material Processing for Solar Energy*, vol. *8473*. SPIE, Bellingham, WA pp. 72, **2012**.
[22] B. Zieliński, B. O'Sullivan, S. Singh, A. U. de Castro, Y. Li, S. Jambaldinni, M. Debucquoy, R. Mertens, J. Poortmans, *Sol. Energy Mater. Sol. Cells* **2017**, *163*, 66.
[23] B. Deal, M. Sklar, *J. Electrochem. Soc.* **1965**, *112*, 430.
[24] B. E. Deal, A. Grove, *J. Appl. Phys.* **1965**, *36*, 3770.
[25] X. G. Zhang, in , Springer, New York **2007**, pp. 131–132.
[26] K. R. Williams, K. Gupta, M. Wasilik, *J. Microelectromech. Syst.* **2003**, *12*, 761.
[27] C. Ho, J. Plummer, *J. Electrochem. Soc.* **1979**, *126*, 1516.
[28] E. Biermann, H. H. Berger, P. Linke, B. Müller, *J. Electrochem. Soc.* **1996**, *143*, 1434.
[29] J. S. Yuan, J. J. Liou, in *Semiconductor Device Physics and Simulation*, Plenum Press, New York **1998**, pp. 155–156.
[30] M. Hassan, M. Dahlinger, J. R. Köhler, R. Zapf-Gottwick, J. H. Werner, *Materials* **2021**, *14*, 2322.
[31] V. D. Mihailetchi, H. Chu, J. Lossen, R. Kopecek, *IEEE J. Photovolt.* **2018**, *8*, 435.
[32] V. V. Kuruganti, D. Wurmbrand, T. Buck, S. Seren, M. Zeman, O. Isabella, F. Geml, H. Plagwitz, B. Terheiden, V. D. Mihailetchi, *Sol. Energy Mater. Sol. Cells* **2023**, *251*, 112111.
[33] C.-C. Yen, A. K. Singh, Y.-M. Chung, H.-Y. Chou, D.-S. Wuu, *Crystals* **2023**, *13*, 336.
[34] T. Kamins, T. Kamins, in *Polycrystalline Silicon for Integrated Circuits and Displays*, Kluwer Academic, United States **1998**, pp. 123–162.
[35] H. Kang, in *IOP Conference Series: Earth and Environmental Science*, vol. *726*, IOP Publishing, Bristol, England pp. 012001, **2021**.
[36] S. Sharbaf Kalaghichi, J. Hoß, R. Zapf-Gottwick, J. H. Werner, *Solar* **2023**, *3*, 362.
[37] M. Tilli, M. Paulasto-Kröckel, M. Petzold, H. Theuss, T. Motooka, V. Lindroos, in *Handbook of Silicon Based MEMS Materials and Technologies*, Elsevier, Amsterdam **2020**, pp. 195–196.
[38] A. Chaudhary, J. Hoß, J. Lossen, F. Huster, R. Kopecek, R. van Swaaij, M. Zeman, *Phys. Status Solidi A* **2021**, *218*, 2100243.